

Influence of lattice termination on the edge states of the quantum spin Hall insulator monolayer $1T'$ -WTe₂

Alexander Lau,¹ Rajyavardhan Ray,^{2,3} Dániel Varjas,^{1,4} and Anton R. Akhmerov¹

¹*Kavli Institute of Nanoscience, Delft University of Technology, P.O. Box 4056, 2600 GA Delft, The Netherlands*

²*Institute for Theoretical Solid State Physics, IFW Dresden, Helmholtzstr. 20, 01069 Dresden, Germany*

³*Dresden Center for Computational Materials Science (DCMS), TU Dresden, 01062 Dresden, Germany*

⁴*QuTech, Delft University of Technology, P.O. Box 4056, 2600 GA Delft, The Netherlands*



(Received 14 January 2019; published 28 May 2019)

We study the influence of sample termination on the electronic properties of the novel quantum spin Hall insulator monolayer $1T'$ -WTe₂. For this purpose, we construct an accurate, minimal four-orbital tight-binding model with spin-orbit coupling by employing a combination of density-functional theory calculations, symmetry considerations, and fitting to experimental data. Based on this model, we compute energy bands and two-terminal conductance spectra for various ribbon geometries with different terminations, with and without a magnetic field. Because of the strong electron-hole asymmetry, we find that the edge Dirac point is buried in the bulk bands for most edge terminations. In the presence of a magnetic field, an in-gap edge Dirac point leads to exponential suppression of conductance as an edge Zeeman gap opens, whereas the conductance stays at the quantized value when the Dirac point is buried in the bulk bands. Finally, we find that disorder in the edge termination drastically changes this picture: the conductance of a sufficiently rough edge is uniformly suppressed for all energies in the bulk gap regardless of the orientation of the edge.

DOI: [10.1103/PhysRevMaterials.3.054206](https://doi.org/10.1103/PhysRevMaterials.3.054206)

I. INTRODUCTION

Quantum spin Hall (QSH) insulators are two-dimensional (2D) materials with a pair of counterpropagating, helical electronic modes along their edges protected from backscattering by time-reversal symmetry [1–6]. They represent celebrated examples of topological insulators [7–10] and have a nonzero \mathbb{Z}_2 topological invariant ν . Their hallmark is a quantized electronic conductance of $G = 2e^2/h$ as a consequence of the eponymous quantum spin Hall effect. More specifically, each of the two oppositely spin-polarized, conducting edge channels contributes one conductance quantum e^2/h . This is a robust feature since backscattering between the two edge channels is forbidden by time-reversal symmetry. The described robustness, however, is expected to break down once time-reversal symmetry is broken, for instance, by a magnetic field.

Experimental efforts in realizing QSH insulators have mostly focused on quantum-well heterostructures based on three-dimensional semiconductors such as HgTe/CdTe or InAs/GaSb quantum wells [6,11–15]. Recently, technological advances in the preparation of monolayer materials have shifted the focus to truly 2D materials as platforms for QSH insulators [16–19]. Those materials include the graphene descendants silicene, germanene, and stanene [18,20,21], as well as the related bismuthene [22].

Another materials class that has attracted attention in this context comprises the single-layer transition metal dichalcogenides [16,23–32]. Specifically, monolayer WTe₂ has been identified theoretically to realize a QSH phase [16,33–35], and various experiments have verified its key features: an insulating bulk, the presence of conducting edge channels,

and a quantized electronic conductance of $2e^2/h$ over a large range of temperatures [36–42]. Furthermore, a magnetic field has been shown to lead to a breakdown of conductance in the investigated samples [42]. This suggests the opening of a Zeeman-type gap in the edge-state spectrum, contrary to other QSH insulator candidate materials [14,15,43]. It remains elusive, however, as to whether the presence of a Zeeman gap is a generic feature of single-layer WTe₂, or which type of edge terminations shows such a gap. To answer this question on a theoretical footing, an accurate low-energy lattice model is required.

In this article, we study the electronic properties of monolayer WTe₂ in the framework of a minimal four-orbital tight-binding model with spin-orbit coupling (SOC). In order to obtain an accurate low-energy description, we derive our model using a hybrid approach that combines density-functional theory (DFT) calculations, symmetry considerations, and experimental data from angle-resolved photoemission spectroscopy (ARPES). We first show that our model captures all the essential features that contribute to the nontrivial topology of the material. When applied to different nanoribbon geometries, this model provides a qualitative understanding of the influence of a magnetic field and of edge disorder: we find that the exponential suppression of conductance, associated with an edge Zeeman gap, is observed only for sufficiently clean edges that feature an in-gap edge Dirac point.

II. TIGHT-BINDING MODEL FOR MONOLAYER WTe₂

WTe₂ is a member of the transition metal dichalcogenide family of materials. Single layers in this materials class

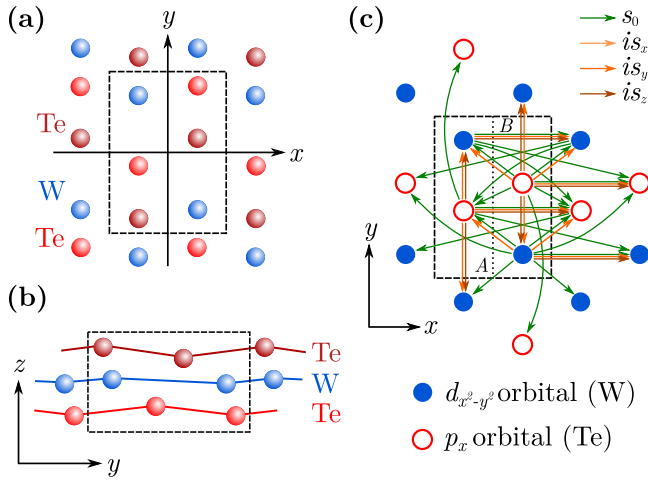


FIG. 1. Lattice and tight-binding model of WTe_2 : (a) top view of the lattice; (b) side view of the lattice. The dashed box indicates the six-site unit cell. (c) Reduced four-site lattice used for the tight-binding model with sublattices A and B indicated. The arrows depict the hopping terms (s_0) and the SOC terms ($s_{x,y,z}$) of the model. We provide a more detailed schematic in the Supplemental Material [47].

crystallize in a variety of polytypic structures such as the hexagonal $2H$, the tetragonal $1T$, and the distorted $1T'$ structure [16,44,45]. While the former represent trivial semiconductors, the $1T'$ configuration gives rise to 2D QSH insulators [16]. Furthermore, monolayer WTe_2 is the only member of this materials class that is known to realize the topologically nontrivial $1T'$ structure as its stable ground state [16,24,25,46].

The crystal structure is generated from the tetragonal $1T$ configuration by a lattice distortion [16,44,45]: the original $1T$ configuration is composed of three hexagonal layers in rhombohedral ABC stacking with one W layer sandwiched between two Te layers. A structural distortion then shifts the W atoms along the b direction to form zigzag chains. At the same time, the three atomic sheets of the lattice are buckled in the out-of-plane direction. The resulting $1T'$ structure has a rectangular unit cell, containing two W sites and four Te sites. We show a top view and a side view of the lattice in Figs. 1(a) and 1(b), respectively.

The lattice distortion of the $1T'$ configuration is the key ingredient to the nontrivial topology [16,33] of WTe_2 . It enlarges the unit cell and leads to a reconstruction of the electronic bands in the 2D Brillouin zone. As a consequence, a band inversion takes place at the Γ point [16,33]. In contrast to other QSH insulator materials, this band inversion is *not* induced by SOC. In fact, theoretical calculations show that the respective bands are inverted already in the nonrelativistic limit, i.e., when SOC is neglected. The corresponding “spinless” band structure, however, does not have a full bulk energy gap. Instead, it realizes a 2D type-II Dirac semimetal due to the presence of two tilted, unpinned Dirac cones near the Γ point, protected by a glide reflection symmetry [48]. Recovering the spin degree of freedom by including SOC then lifts the degeneracy at the Dirac cones and leads to a sizable, indirect bulk energy gap.

Our aim is to investigate the electronic properties of WTe_2 in ribbons with arbitrary terminations including rough edges.

So far, theoretical studies of this material have mostly been limited to DFT calculations and low-energy $\mathbf{k} \cdot \mathbf{p}$ models [16,23,27,28,33–35]. For the former, it is computationally expensive to model large ribbons with disordered edges. The latter, on the other hand, is a long wavelength theory and does not capture geometric details at small length scales. In the following, we therefore construct a minimal tight-binding model suitable for studying the low-energy electronic properties of monolayer WTe_2 on arbitrarily terminated lattices.

Effective tight-binding models for monolayer WTe_2 have been derived from DFT calculations in Refs. [48,49]. Such models are typically extracted from DFT via a projection of the DFT wave functions onto a subset of atomic orbitals. Fully relativistic DFT calculations, which take into account the spin degree of freedom of the electrons, however, have not been able to reproduce quantitatively the size of the energy gap and the dispersion of the valence band close to the Fermi level, as measured in scanning tunneling spectroscopy and ARPES experiments [35,37,40,50]. To overcome this issue, we choose to take an alternative route by combining scalar-relativistic DFT calculations with symmetry considerations and data from ARPES, thereby obtaining an accurate bulk model.

A. DFT calculations and optimized Wannier fit

As a first step of our construction, we perform DFT calculations of the electronic structure of freestanding $1T'$ - WTe_2 monolayers in an all-electron full-potential local-orbital basis using the FPLO code [51,52]. We employ the PBE implementation [53] of the generalized gradient approximation (GGA) including scalar relativistic corrections. For the numerical integration, we use a $(12 \times 12 \times 1)$ \mathbf{k} mesh in the full Brillouin zone along with the linear tetrahedron method. Moreover, we take the lattice parameters and the atomic positions from Ref. [54].

In agreement with the literature [33,48], we find that the four bands closest to the Fermi level are composed mainly of contributions from two $3d_{x^2-y^2}$ -type orbitals centered at W sites and from two $5p_x$ -type orbitals centered at a subset of Te sites. Hence, a tight-binding model consisting of these four orbitals represents a suitable minimal model. We therefore construct localized Wannier orbitals from the two W- d and two Te- p orbitals [see Fig. 1(c)], and compute the corresponding real-space overlaps to obtain the tight-binding parameters for our minimal four-orbital model. Figure 2 shows the resulting tight-binding bands, corresponding to the Wannier fit, along with the DFT band structure.

The Wannier tight-binding model reproduces the key features of the DFT band structure close to the Fermi level reasonably well, including the tilted type-II Dirac cones near the Γ point. It turns out, however, that the small number of orbitals requires the inclusion of a large number of neighbors in the Wannier fit. At the same time, irrespective of the number of neighbors, the location of the Dirac point in \mathbf{k} space is slightly shifted compared to the DFT band structure. To obtain a more accurate low-energy description, we therefore adopt a hybrid approach: we take the onsite energies and the largest hopping parameters (≥ 0.4 eV) from DFT, while we treat others above a certain energy cutoff as effective hopping parameters (see

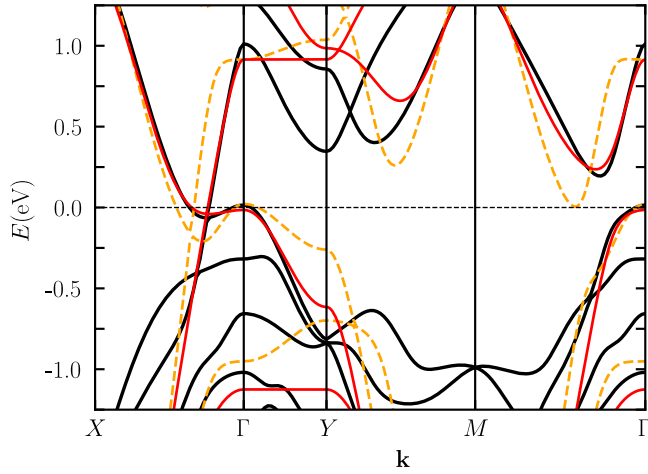


FIG. 2. Energy bands without SOC along high-symmetry lines in the Brillouin zone: DFT calculations (solid black lines), Wannier tight-binding fit (dashed orange lines), and energy bands from the optimized tight-binding fit (solid red lines).

Supplemental Material for details [47]). Finally, we optimize the latter to fit the DFT energy bands close to the Fermi level. In the Supplemental Material [47], we demonstrate that such an optimization is indeed needed to not overestimate the SOC terms in the next step and that this does not affect the final conclusions of our study.

Figure 1(c) illustrates the hopping terms of the resulting tight-binding Hamiltonian without SOC. We provide a more detailed depiction in the Supplemental Material [47]. The corresponding Bloch Hamiltonian is

$$\begin{aligned}
 H_0 = & \left[\frac{\mu_p}{2} + t_{px} \cos(ak_x) + t_{py} \cos(bk_y) \right] \Gamma_1^- \\
 & + \left[\frac{\mu_d}{2} + t_{dx} \cos(ak_x) \right] \Gamma_1^+ \\
 & + t_{dAB} e^{-ibk_y} (1 + e^{iak_x}) e^{i\mathbf{k} \cdot \Delta_1} \Gamma_2^+ \\
 & + t_{pAB} (1 + e^{iak_x}) e^{i\mathbf{k} \cdot \Delta_2} \Gamma_2^- \\
 & + t_{0AB} (1 - e^{iak_x}) e^{i\mathbf{k} \cdot \Delta_3} \Gamma_3 \\
 & - 2it_{0x} \sin(ak_x) [e^{i\mathbf{k} \cdot \Delta_4} \Gamma_4^+ + e^{-i\mathbf{k} \cdot \Delta_4} \Gamma_4^-] \\
 & + t_{0ABx} (e^{-iak_x} - e^{2iak_x}) e^{i\mathbf{k} \cdot \Delta_3} \Gamma_3 \\
 & + \text{H.c.}
 \end{aligned} \quad (1)$$

The 4×4 matrices Γ_i are linear combinations of products $\tau_j \sigma_i$ of Pauli matrices (see Supplemental Material [47]) acting in orbital space with respect to the basis $\{d_{\mathbf{k}Ad_s}, d_{\mathbf{k}Ap_s}, d_{\mathbf{k}Bd_s}, d_{\mathbf{k}Bp_s}\}$, where $d_{\mathbf{k}cls}$ annihilates an electron with momentum \mathbf{k} , spin- S_z eigenvalue $s = \uparrow, \downarrow$ and orbital $l = p, d$ (Te, W) in sublattice $c = A, B$. We have further defined $\Delta_1 = \mathbf{r}_{Ad} - \mathbf{r}_{Bd}$, $\Delta_2 = \mathbf{r}_{Ap} - \mathbf{r}_{Bp}$, $\Delta_3 = \mathbf{r}_{Ad} - \mathbf{r}_{Bp}$, and $\Delta_4 = \mathbf{r}_{Ad} - \mathbf{r}_{Ap}$, where the vector \mathbf{r}_{cl} denotes the position of the corresponding lattice site, associated with an orbital l in sublattice c , in the unit cell. The lattice constants are $a = 3.477 \text{ \AA}$ and $b = 6.249 \text{ \AA}$.

Figure 2 shows a comparison of the energy bands of the optimized tight-binding model with the DFT bands close to the Fermi level. We find that the model indeed gives an

accurate description of the DFT bands around the Fermi level and correctly reproduces the positions of the Dirac points.

B. Spin-orbit coupling from symmetries

Having established an accurate minimal tight-binding model without SOC, we now add a set of symmetry-allowed SOC terms to our model. The symmetry group of the WTe_2 lattice is generated by the following operations [48]: lattice translations $T(\mathbf{a})$ and $T(\mathbf{b})$, where $\mathbf{a} = a\hat{x}$ and $\mathbf{b} = b\hat{y}$ with unit vectors \hat{x}, \hat{y} ; a glide reflection $\tilde{M}_x = T(\mathbf{a}/2)M_x$ with the regular reflection M_x about the yz plane acting as $M_x: (x, y, z) \rightarrow (-x, y, z)$; inversion \mathcal{I} acting as $\mathcal{I}: (x, y, z) \rightarrow (-x, -y, -z)$; and time reversal Θ . In the basis of the Hamiltonian in Eq. (1), the matrix representations of the symmetry operations are $\hat{\Theta} = is_y \Gamma_0 K$ with complex conjugation K , $\hat{\mathcal{I}} = s_0 \tau_1 \sigma_3$, and $\hat{M}_x = is_x \tau_0 \sigma_3$ for the nontranslational component of \tilde{M}_x .

By making use of the PYTHON package QSYMM [55], we generate all symmetry-allowed SOC terms up to nearest neighbors and also include symmetry-allowed, next-nearest neighbor SOC terms in the x direction. Figure 1(c) illustrates all SOC terms taken into account. The Bloch Hamiltonian of the final tight-binding model with SOC is $H(\mathbf{k}) = s_0 H_0(\mathbf{k}) + H_{\text{SOC}}(\mathbf{k})$, with

$$\begin{aligned}
 H_{\text{SOC}} = & [(\lambda_{dx}^z s_z + \lambda_{dx}^y s_y) \sin(ak_x)] \Gamma_5^+ \\
 & + [(\lambda_{px}^z s_z + \lambda_{px}^y s_y) \sin(ak_x)] \Gamma_5^- \\
 & - i\lambda_{0AB}^y s_y (1 + e^{iak_x}) e^{i\mathbf{k} \cdot \Delta_3} \Gamma_6 \\
 & - i(\lambda_0^z s_z + \lambda_0^y s_y) (e^{i\mathbf{k} \cdot \Delta_4} \Gamma_4^+ - e^{-i\mathbf{k} \cdot \Delta_4} \Gamma_4^-) \\
 & - i(\lambda_0^z s_z + \lambda_0^y s_y) \\
 & \times (e^{-ibk_y} e^{i\mathbf{k} \cdot \Delta_4} \Gamma_4^+ - e^{ibk_y} e^{-i\mathbf{k} \cdot \Delta_4} \Gamma_4^-) \\
 & + \text{H.c.},
 \end{aligned} \quad (2)$$

where the $s_{x,y,z}$ are Pauli matrices acting in spin space and s_0 is the corresponding identity.

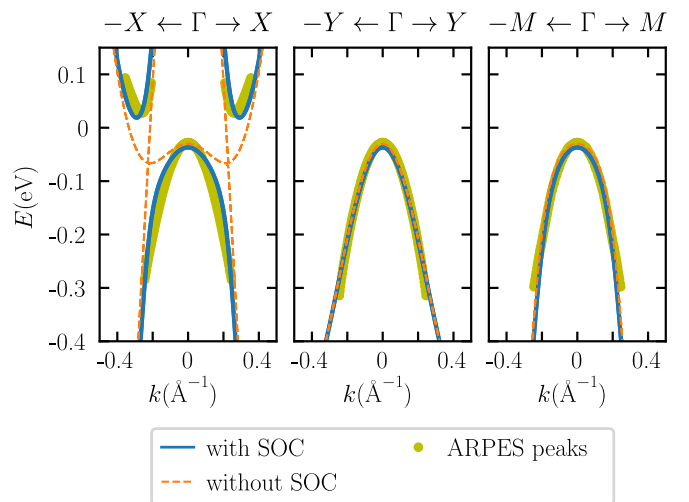


FIG. 3. Energy bands of the final tight-binding model with and without SOC ($\lambda_i = 0$) compared with intensity peaks from ARPES measurements (courtesy of Ref. [40]).

TABLE I. Tight-binding and lattice parameters of the final four-orbital model.

μ_p	-1.75 eV	λ_{0AB}^y	0.011 eV
μ_d	0.74 eV	λ_0^y	0.051 eV
t_{px}	1.13 eV	λ_0^z	0.012 eV
t_{dx}	-0.41 eV	$\lambda_0'^y$	0.050 eV
t_{pAB}	0.40 eV	$\lambda_0'^z$	0.012 eV
t_{dAB}	0.51 eV	λ_{px}^y	-0.040 eV
t_{0AB}	0.39 eV	λ_{px}^z	-0.010 eV
t_{0ABx}	0.29 eV	λ_{dx}^y	-0.031 eV
t_{0x}	0.14 eV	λ_{dx}^z	-0.008 eV
t_{py}	0.13 eV		
a	3.477 Å	b	6.249 Å
\mathbf{r}_{Ad}	(-0.25a, 0.32b)	\mathbf{r}_{Bp}	(0.25a, 0.07b)
\mathbf{r}_{Ap}	(-0.25a, -0.07b)	\mathbf{r}_{Bd}	(0.25a, -0.32b)

We obtain the parameters of the SOC terms in Eq. (2) by fitting to ARPES data close to the Fermi level from Ref. [40]. The large number of free parameters in the fit is handled using a LASSO regression analysis (see Supplemental Material [47] for details). As illustrated in Fig. 3, the energy bands of the resulting model provide an excellent fit to the ARPES data. We have tabulated the parameter values of the final Hamiltonian in Table I.

Figure 4 shows the full band structure of the tight-binding model. Due to the simultaneous presence of time-reversal and inversion symmetry, all bands are two-fold degenerate. Most importantly, the model has an indirect energy gap of $\Delta E = 56$ meV, compatible with experiments [37,40,50]. Moreover, close to the Fermi level, the dispersion of our model matches experimental results [40,50] by construction. An analysis of the parities ξ of the states at the four time-reversal invariant momenta Γ , X , Y , and M shows that the lowest conduction band and the lowest valence band in our model are inverted at Γ [see Fig. 4(a)], as expected from DFT calculations [33].

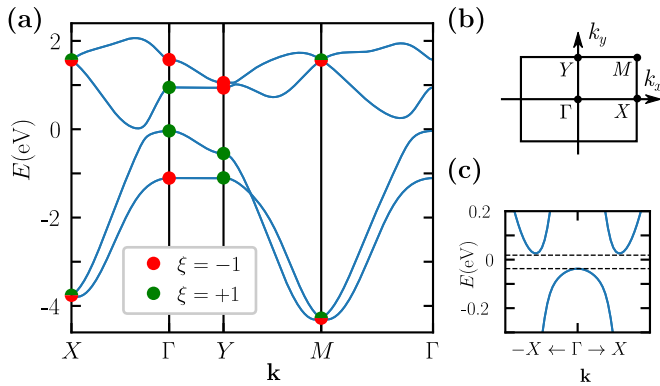


FIG. 4. Bulk energy bands of the monolayer-WTe₂ tight-binding model: (a) along high-symmetry lines in the Brillouin zone. We have indicated the parities ξ of states at the time-reversal invariant momenta. (b) Bulk Brillouin zone. (c) Energy bands close to Γ along ΓX in a small energy window around the bulk energy gap. The dashed lines indicate the edges of the bulk energy gap.

Finally, we compute the \mathbb{Z}_2 invariant of the model at half filling using the parities of occupied states at time-reversal invariant momenta [56]. We obtain $\nu = 1$, confirming that our model realizes a QSH insulator, in agreement with experiments [40,42].

III. FINITE GEOMETRIES WITHOUT MAGNETIC FIELD

With an accurate bulk tight-binding model at hand, we now study how its low-energy electronic properties depend on the specific termination in a finite geometry. Obtaining an equally accurate model of the edge is not possible from the available experimental data. Nevertheless, using a truncated bulk Hamiltonian is sufficient to understand the qualitative effects of various lattice terminations (the limitations of this approach are discussed in the Supplemental Material [47]). For that purpose, we put our monolayer-WTe₂ model into different ribbon geometries, each of which has only a single direction \mathbf{d} of translational symmetry. In this direction, we impose periodic boundary conditions. In the perpendicular direction, in which the ribbon has a width W , we use open boundary conditions. Here, we discuss four representative examples of terminations, which are depicted in the insets of Fig. 5. For these systems, we choose W to be between 80 and 100 unit cells. In the following, we present energy spectra and two-terminal conductance calculations for these geometries, for now, without magnetic field.

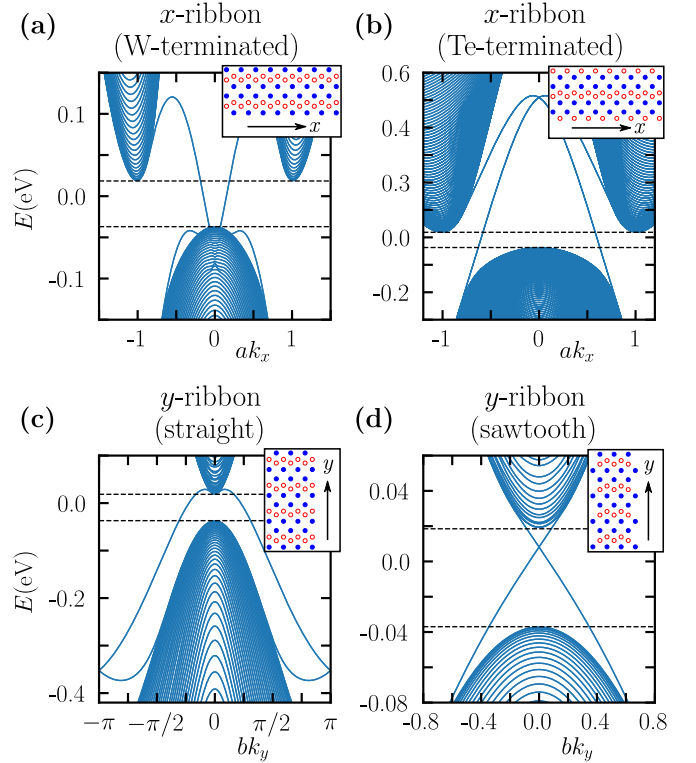


FIG. 5. Energy dispersion of ribbons with different terminations close to the Fermi level without magnetic field. The dashed lines indicate the bulk energy gap. The insets show the respective terminations using the same color code as in Fig. 1(c).

A. Energy spectra

As we have shown in the previous section, our model realizes a 2D topological insulator. Hence, for any finite geometry, isolated bands of helical edge states are expected to connect the bulk valence and conduction bands across the bulk energy gap. To analyze how the dispersion of these edge bands depends on the considered termination, we compute the energy states of the ribbons as a function of the momentum k_{\parallel} parallel to the translationally invariant direction \mathbf{d} . Figure 5 shows the resulting energy spectra close to the Fermi level.

The general observations are the same for all ribbons: two pairs of isolated bands, corresponding to counterpropagating helical edge states, traverse the bulk energy gap. Moreover, these states are spatially separated and localized to opposite edges of the ribbon. This is a hallmark of QSH insulators. The specific edge-state dispersions, however, differ qualitatively.

Figure 5(a) shows the dispersion of a ribbon terminated between the W sites with $\mathbf{d} = \hat{\mathbf{x}}$. This termination has edge energy bands that do not cross each other. In contrast to that, ribbons terminated between Te sites with $\mathbf{d} = \hat{\mathbf{x}}$ have edge bands that cross at the time-reversal invariant edge momentum $k_{\parallel} = k_x = 0$ [see Fig. 5(b)]. The crossing represents a Kramers doublet, or Dirac point, and is protected by time-reversal symmetry. It is, however, energetically far outside the bulk energy gap. We make a similar observation for straight terminations with $\mathbf{d} = \hat{\mathbf{y}}$, as shown in Fig. 5(c). Here, the Dirac point is at $k_{\parallel} = k_y = \pi/b$ and energetically far below the bulk energy gap.

The situation is different for ribbons with $\mathbf{d} = \hat{\mathbf{y}}$ and a sawtooth termination [see Fig. 5(d)]. Again, we find two pairs of helical edge bands traversing the bulk energy gap, but in this geometry the bands cross inside the bulk energy gap at the time-reversal invariant edge momentum $k_{\parallel} = k_y = 0$: the edge-state spectrum has a so-called *in-gap* Dirac point. In contrast, the edge Dirac points of most terminations, including the ones discussed before, are “hidden” or “buried” [43] in the bulk energy bands. This is due to the strong electron-hole asymmetry of the material. We will see that the distinction between terminations with buried and with in-gap edge Dirac points is crucial in the presence of a magnetic field.

B. Two-terminal conductance

We now look at how the termination of the ribbons affects their transport properties. Specifically, we look into the two-terminal conductance of our systems. For that purpose, we remove the periodic boundary conditions of the ribbon under consideration and attach metallic leads of the same width as the ribbon on each side. This is achieved by shifting the chemical potential deep into the valence band at both ends of the ribbon. The samples considered here have a length L of 200 unit cells. This is of similar magnitude as the edge length of samples studied in experiments with sizes ranging from 60 to 100 nm [42].

We compute the corresponding scattering matrix $S(E)$ as a function of energy E using the quantum transport software package KWANT [57]. The conductance is then given by $G = e^2/h \sum_{nm} |S_{nm}|^2$, where n, m run over all electronic modes in the leads. We show our results for G as a function of E without magnetic field in Fig. 6(a).

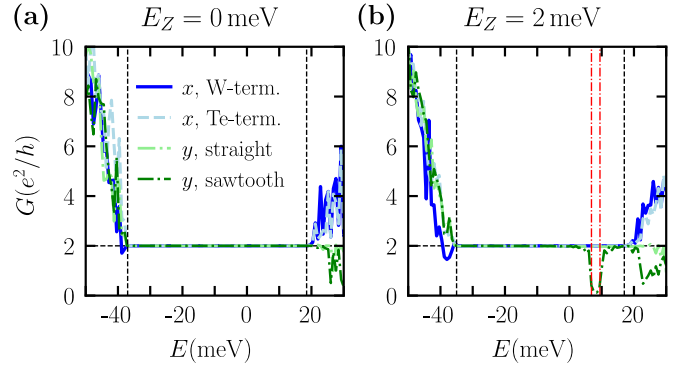


FIG. 6. Two-terminal conductance of differently terminated WTe₂ ribbons: (a) without magnetic field ($E_Z = 0$); (b) with an out-of-plane magnetic field corresponding to $E_Z = 2$ meV ($B = 9.4$ T). The dashed vertical lines indicate the edges of the bulk conduction and of the bulk valence band. We have also indicated the induced edge energy gap of the sawtooth y ribbon by vertical dash-dot lines in red.

IV. FINITE GEOMETRIES WITH MAGNETIC FIELD

We proceed by studying the effect of an out-of-plane magnetic field $\mathbf{B} = B\hat{\mathbf{z}}$ on the edge-state dispersions and on the conductance of monolayer WTe₂. For this purpose, we add an on-site Zeeman term of the form $H_Z = E_Z s_z \Gamma_0$ to the time-reversal symmetric Hamiltonian $H(\mathbf{k})$ of Eqs. (1) and (2), where Γ_0 is the 4×4 identity matrix in orbital space. We establish the relation between the Zeeman energy E_Z and the magnetic field B later on.

Figure 7 shows energy spectra corresponding to the ribbons studied in the previous section under a finite magnetic field. First of all, we observe that the bulk energy gap is slightly smaller. Moreover, we generally find that the degeneracy of edge states localized to opposite boundaries of the ribbon is lifted because of the broken time-reversal symmetry. However, a Zeeman gap opens in the edge-state spectrum only if the lifted degeneracy involves states localized to the same boundary, such as states of a Dirac point. We discuss the implications below.

W-terminated x ribbons do not have a Dirac point in their edge-state spectrum. Consequently, the edge-state dispersion remains gapless even at finite magnetic fields, as we show in Fig. 7(a). In contrast to that, the spectra of Te-terminated x ribbons and of straight y ribbons do have an edge Dirac point far outside the bulk energy gap. These Dirac points are gapped out by the magnetic field, but lead only to a “warped” Zeeman gap in the energy spectrum. In other words, bulk valence and conduction bands are no longer connected by edge bands, but there still exist electronic states (bulk and/or edge states) for any fixed energy E [see Figs. 7(b)–7(c)]. Due to the nature of the edge energy gap, the ribbons are effectively still gapless in the presence of a magnetic field. Hence, the edge Zeeman gap, without other states crossing it, must be inside the bulk energy gap to suppress electronic transport.

The sawtooth y termination satisfies this requirement with an edge Zeeman gap at $k_y = 0$ inside the bulk energy gap, which we show in Fig. 7(d). This behavior is fundamentally different from the other ribbon geometries: there now exists a

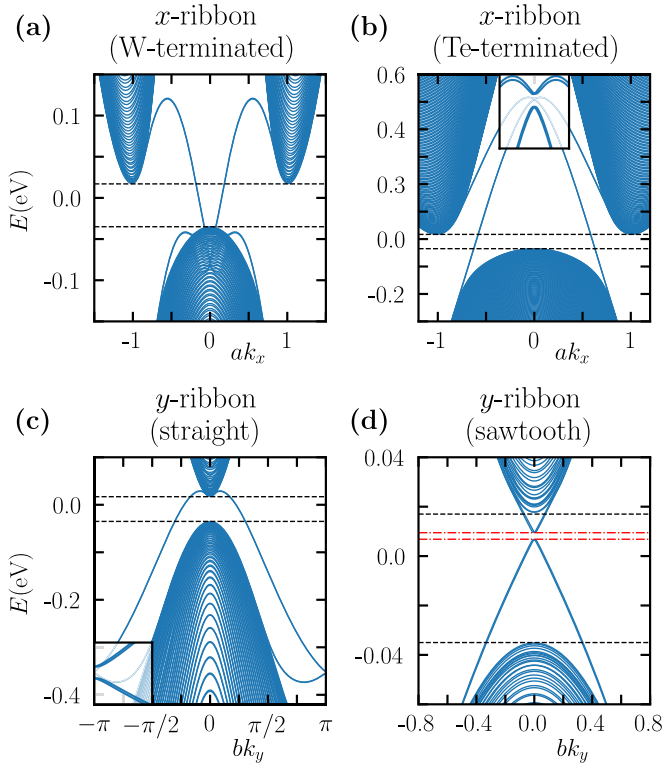


FIG. 7. Energy dispersion of ribbons with different terminations close to the Fermi level with an out-of-plane magnetic field corresponding to $E_Z = 2$ meV ($B = 9.4$ T). The dashed lines indicate the edges of the bulk energy gap. We have also highlighted the edge energy gap of the sawtooth y ribbon by red dash-dot lines. The insets in (b) and (c) show magnified spectra around the gapped edge Dirac points.

small energy window inside the bulk energy gap without any available states. Moreover, from the size of the Zeeman gap and from the effective out-of-plane g factor [42], we estimate the relation between the Zeeman energy E_Z and the magnetic field strength B to be $B[\text{T}] \approx 4.7 E_Z [\text{meV}]$ (see Supplemental Material [47] for details).

Also the conductance reflects the qualitative difference of edge-state spectra between different ribbons. Figure 6(b) shows the conductance corresponding to the ribbons analyzed above as a function of energy under magnetic field. We still find $G = 2e^2/h$ throughout the bulk energy gap for the two x ribbons and for the straight y ribbon. The conductance remains quantized because the considered edges preserve translational symmetry. On the contrary, the conductance of the sawtooth y ribbon drops to zero around the Dirac-point energy, while being quantized to $2e^2/h$ outside this small energy window. Furthermore, by comparing it to the edge-state spectrum in Fig. 7(d), we directly attribute the position and the width of the conductance drop to the presence of an edge energy gap.

V. RIBBONS WITH DISORDERED EDGES UNDER MAGNETIC FIELD

The edges of typical samples used in experiments on 2D monolayer materials are highly irregular, i.e., they have cracks, steps, or bumps [42,50]. Hence, the samples are no

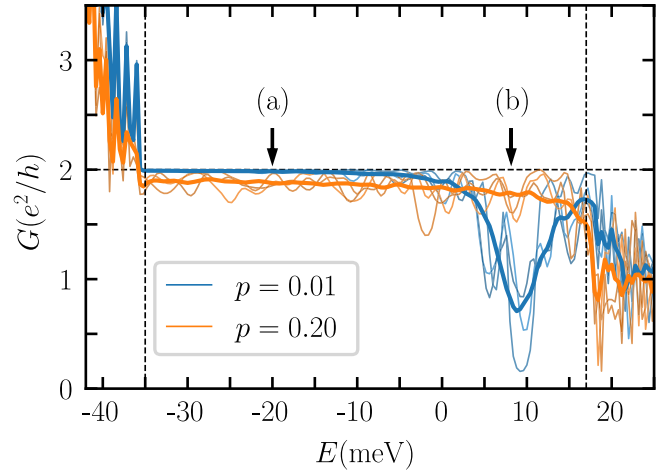


FIG. 8. Conductance G of sawtooth y ribbons under magnetic field [$E_Z = 2$ meV ($B = 9.4$ T)] as a function of energy E for different disorder strengths p . Thin lines represent single samples with different realizations of disordered edges at fixed p . Bold lines correspond to the average conductance G_{av} for an ensemble of 50 disorder realizations. The vertical dashed lines indicate the edges of the bulk energy gap. The black arrows point to the energy values considered in Figs. 9(a) and 9(b), respectively.

longer translationally invariant along their boundary, enabling backscattering of edge states when time-reversal symmetry is broken. We model a rough edge by the boundary following a random walk with a step appearing at every site with probability p (see Supplemental Material [47] for details). The parameter p is therefore a measure of disorder strength.

Figure 8 shows the conductance G of single sawtooth y ribbons and the corresponding disorder-averaged conductance G_{av} for different disorder strengths p . For a given disordered sample the conductance fluctuates considerably as a function of energy. We find that the characteristic exponential suppression of conductance is visible only in the low-disorder regime for edges with an in-gap Dirac point. This is also reflected in a dip of the average conductance G_{av} around the Dirac-point energy. Away from a Dirac point, however, G_{av} shows only a weak energy dependence. The height of this conductance plateau decreases with increasing disorder p due to the onset of Anderson localization. On the other hand, strong disorder removes the conductance suppression in the Zeeman gap and the conductance shows the same plateau behavior throughout the entire bulk energy gap. In other words, the edge energy gap effectively closes for strong disorder, thereby becoming statistically indistinguishable from an edge without an in-gap Dirac point (see Fig. 8).

We observe a qualitatively similar behavior for the conductance as a function of the Zeeman energy E_Z (see Fig. 9). For weak disorder, the conductance at the Dirac point decays exponentially to zero, which is in agreement with experimental results [42], whereas it decays much slower in the plateau regime. As expected from Anderson localization, the conductance in the plateau regime is suppressed with increasing disorder. Contrary to this, the conductance at the Dirac point is *enhanced* by the edge disorder. This happens because localized states, whose finite overlap with the leads enables

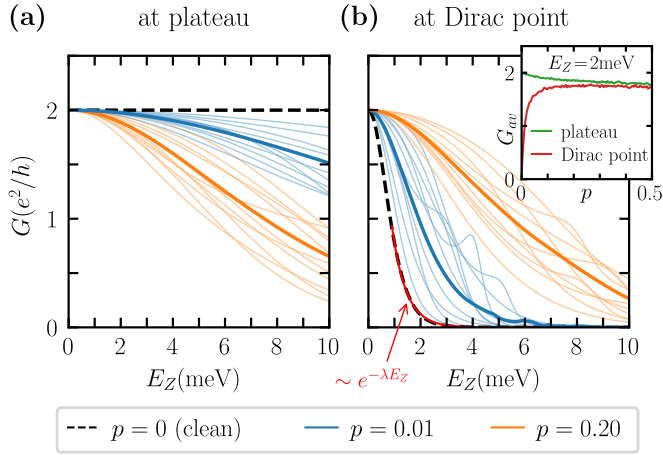


FIG. 9. Conductance G of sawtooth y ribbons at fixed energies E as a function of the disorder strength p and the Zeeman energy E_Z : (a) at the plateau ($E = -20$ meV); (b) at the Dirac point ($E = 8.15$ meV) with exponential decay in the clean limit ($\lambda = 1.8$ meV $^{-1}$). Thin lines correspond to single samples with particular realizations of edge disorder at fixed p . Bold lines depict the average conductance G_{av} over 50 disorder realizations. The inset in (b) shows the average conductance as a function of p at fixed $E_Z = 2$ meV ($B = 9.4$ T).

transport, fill the Zeeman gap. Moreover, as we show in the inset of Fig. 9(b), the $G_{av}(p)$ curves of the two regimes gradually approach each other until they coincide for sufficiently strong disorder.

We have seen that, in the clean limit, there are two qualitatively different behaviors in the presence of magnetic field. For samples with an in-gap edge Dirac point, the conductance drops to zero around the energy of the Dirac point. For terminations with a buried Dirac point, the conductance is constant and equal to $2e^2/h$. We observe the same plateau behavior of quantized conductance also for terminations with in-gap Dirac points if the conductance is measured away from the Dirac-point energy. While this is qualitatively reproduced in samples with weak edge disorder, strong disorder washes out the Zeeman gap. The experiments in Ref. [42] have observed exponential conductance suppression. Therefore, we expect the edges of the samples investigated there to contain sufficiently long straight segments.

VI. CONCLUSION

We have studied edge-state dispersions and two-terminal conductance of the quantum spin Hall insulator monolayer $1T'$ -WTe $_2$ in a four-orbital tight-binding model in various geometries. We have derived our model combining density-functional theory calculations, symmetry considerations, and photoemission spectroscopy data. By construction, our model provides a better fit to experimental results than previous approaches. We use this model to study the effects of magnetic

field and disorder on differently terminated nanoribbons. Without a magnetic field, the topological nature of the system gives rise to helical edge states independent of the system geometry. Nonetheless, we find that the edge-state dispersion strongly depends on the termination: for some terminations there is an in-gap edge Dirac point, whereas for others the edge Dirac point is buried in the bulk energy bands. This has important consequences for the conductance in the time-reversal symmetry-broken regime.

For terminations with a buried edge Dirac point, the conductance fluctuates around a plateau, the value of which decreases slowly with magnetic field and with the magnitude of disorder along the edge. For terminations with an in-gap Dirac point, there is an additional suppression of conductance around the energy of the Dirac point due to a Zeeman gap. There, the conductance exponentially decays to zero as a function of the magnetic field. We further observe that the conductance is gradually enhanced around the Dirac-point energy as the edge disorder is increased. Hence, the characteristic exponential suppression of conductance is only visible for sufficiently clean edge terminations with an in-gap Dirac point.

Our results help to understand recent experimental findings in $1T'$ -WTe $_2$ monolayers. Moreover, the tight-binding model derived in this work provides a minimal but realistic low-energy description to study other promising directions in this materials class, such as the $1T'$ phase [24,25] in WSe $_2$ or superconductivity in $1T'$ -WTe $_2$ monolayers [29,30].

All files and data used in this study are available in the repository at Ref. [58].

ACKNOWLEDGMENTS

We thank L. Wang, V. Fatemi, M. Wimmer, M. Richter, K. Koepnick, and J. Facio for fruitful discussions and helpful comments. We thank S. Tang and Z.-X. Shen for providing access to their experimental data. R.R. thanks U. Nitzsche for technical support. This work was supported by ERC Starting Grant 638760, the Netherlands Organisation for Scientific Research (NWO/OCW), and the U.S. Office of Naval Research. R.R. acknowledges financial support from the European Union (ERDF) and the Free State of Saxony via the ESF projects 100231947 and 100339533 (Young Investigators Group “Computer Simulations for Materials Design” - CoSiMa).

A.A. initiated and oversaw the project. A.L. and D.V. formulated the minimal model from symmetries. R.R. carried out the density-functional theory calculations. A.L. and R.R. performed the fitting of the tight-binding parameters. A.L. performed the conductivity and energy spectra calculations for the tight-binding model. D.V. took part in modeling the disordered edges. A.L., D.V., R.R., and A.A. contributed to interpreting the results and writing the manuscript.

[1] C. L. Kane and E. J. Mele, Quantum Spin Hall Effect in Graphene, *Phys. Rev. Lett.* **95**, 226801 (2005).

[2] C. L. Kane and E. J. Mele, \mathbb{Z}_2 Topological Order and the Quantum Spin Hall Effect, *Phys. Rev. Lett.* **95**, 146802 (2005).

- [3] B. A. Bernevig and S.-C. Zhang, Quantum Spin Hall Effect, *Phys. Rev. Lett.* **96**, 106802 (2006).
- [4] D. N. Sheng, Z. Y. Weng, L. Sheng, and F. D. M. Haldane, Quantum spin Hall effect and topologically invariant Chern numbers, *Phys. Rev. Lett.* **97**, 036808 (2006).
- [5] T. Fukui and Y. Hatsugai, Topological aspects of the quantum spin-Hall effect in graphene: Z_2 topological order and spin Chern number, *Phys. Rev. B* **75**, 121403(R) (2007).
- [6] M. König *et al.*, Quantum spin Hall insulator state in HgTe quantum wells, *Science* **318**, 766 (2007).
- [7] M. Z. Hasan and C. L. Kane, Colloquium: Topological insulators, *Rev. Mod. Phys.* **82**, 3045 (2010).
- [8] X.-L. Qi and S.-C. Zhang, Topological insulators and superconductors, *Rev. Mod. Phys.* **83**, 1057 (2011).
- [9] S. Ryu, A. P. Schnyder, A. Furusaki, and A. W. W. Ludwig, Topological insulators and superconductors: Tenfold way and dimensional hierarchy, *New J. Phys.* **12**, 065010 (2010).
- [10] A. W. W. Ludwig, Topological phases: Classification of topological insulators and superconductors of noninteracting fermions, and beyond, *Phys. Scripta T* **168**, 014001 (2015).
- [11] I. Knez, R.-R. Du, and G. Sullivan, Evidence for Helical edge Modes in Inverted InAs/GaSb Quantum Wells, *Phys. Rev. Lett.* **107**, 136603 (2011).
- [12] D. I. Pikulin and T. Hyart, Interplay of Exciton Condensation and the Quantum Spin Hall Effect in InAs/GaSb Bilayers, *Phys. Rev. Lett.* **112**, 176403 (2014).
- [13] L. Du, I. Knez, G. Sullivan, and R.-R. Du, Robust Helical Edge Transport in Gated InAs/GaSb Bilayers, *Phys. Rev. Lett.* **114**, 096802 (2015).
- [14] E. Y. Ma *et al.*, Unexpected edge conduction in mercury telluride quantum wells under broken time-reversal symmetry, *Nat. Commun.* **6**, 7252 (2015).
- [15] F. Nichele *et al.*, Edge transport in the trivial phase of InAs/GaSb, *New J. Phys.* **18**, 083005 (2016).
- [16] X. Qian, J. Liu, L. Fu, and J. Li, Quantum spin Hall effect in two-dimensional transition metal dichalcogenides, *Science* **346**, 1344 (2014).
- [17] J.-J. Zhou *et al.*, Large-gap quantum spin Hall insulator in single layer bismuth monobromide Bi_4Br_4 , *Nano Lett.* **14**, 4767 (2014).
- [18] M. Ezawa, Monolayer topological insulators: Silicene, germanene, and stanene, *J. Phys. Soc. Jpn.* **84**, 121003 (2015).
- [19] S.-S. Li *et al.*, Robust room-temperature quantum spin Hall effect in methyl-functionalized InBi honeycomb film, *Sci. Rep.* **6**, 23242 (2016).
- [20] C.-C. Liu, W. Feng, and Y. Yao, Quantum Spin Hall Effect in Silicene and Two-Dimensional Germanium, *Phys. Rev. Lett.* **107**, 076802 (2011).
- [21] Y. Xu, B. Yan, H. J. Zhang, J. Wang, G. Xu, P. Tang, W. Duan, and S. C. Zhang, Large-Gap Quantum Spin Hall Insulators in Tin Films, *Phys. Rev. Lett.* **111**, 136804 (2013).
- [22] G. Li, W. Hanke, E. M. Hankiewicz, F. Reis, J. Schafer, R. Claessen, C. Wu, and R. Thomale, Theoretical paradigm for the quantum spin Hall effect at high temperatures, *Phys. Rev. B* **98**, 165146 (2018).
- [23] J.-H. Lee and Y.-W. Son, Reentrant quantum spin Hall states in charge density wave phase of doped single-layer transition metal dichalcogenides, [arXiv:1711.08073](https://arxiv.org/abs/1711.08073).
- [24] M. M. Ugeda *et al.*, Observation of topologically protected states at crystalline phase boundaries in single-layer WSe_2 , *Nat. Commun.* **9**, 3401 (2018).
- [25] P. Chen *et al.*, Quantum-spin-Hall insulator with a large gap: Single-layer $1T'-\text{WSe}_2$, *Nat. Commun.* **9**, 2003 (2018).
- [26] S.-Y. Xu *et al.*, Electrically switchable Berry curvature dipole in the monolayer topological insulator WTe_2 , *Nat. Phys.* **14**, 900 (2018).
- [27] Y. Zhang, J. van den Brink, C. Felser, and B. Yan, Electrically tuneable nonlinear anomalous Hall effect in two-dimensional transition-metal dichalcogenides WTe_2 and MoTe_2 , *2D Mater.* **5**, 044001 (2018).
- [28] L.-K. Shi and J. C. W. Song, Berry curvature switch and magneto-electric effect in WTe_2 monolayer, *Phys. Rev. B* **99**, 035403 (2019).
- [29] V. Fatemi *et al.*, Electrically tunable low-density superconductivity in a monolayer topological insulator, *Science* **362**, 926 (2018).
- [30] E. Sajadi *et al.*, Gate-induced superconductivity in a monolayer topological insulator, *Science* **362**, 922 (2018).
- [31] K. Kang, T. Li, E. Sohn, J. Shan, and K. F. Mak, Observation of the nonlinear anomalous Hall effect in 2D WTe_2 , [arXiv:1809.08744](https://arxiv.org/abs/1809.08744).
- [32] L. Wang, T. O. Rosdahl, and D. Sticlet, Platform for nodal topological superconductors in monolayer molybdenum dichalcogenides, *Phys. Rev. B* **98**, 205411 (2018).
- [33] D.-H. Choe, H.-J. Sung, and K. J. Chang, Understanding topological phase transition in monolayer transition metal dichalcogenides, *Phys. Rev. B* **93**, 125109 (2016).
- [34] H. Xiang *et al.*, Quantum spin Hall insulator phase in monolayer WTe_2 by uniaxial strain, *AIP Adv.* **6**, 095005 (2016).
- [35] F. Zheng *et al.*, On the quantum spin Hall gap of monolayer $1T'-\text{WTe}_2$, *Adv. Mater.* **28**, 4845 (2016).
- [36] Z. Fei *et al.*, Edge conduction in monolayer WTe_2 , *Nat. Phys.* **13**, 677 (2017).
- [37] Z. Y. Jia, Y. H. Song, X. B. Li, K. Ran, P. Lu, H. J. Zheng, X. Y. Zhu, Z. Q. Shi, J. Sun, J. Wen, D. Xing, and S. C. Li, Direct visualization of a two-dimensional topological insulator in the single-layer $1T'-\text{WTe}_2$, *Phys. Rev. B* **96**, 041108(R) (2017).
- [38] L. Peng *et al.*, Observation of topological states residing at step edges of WTe_2 , *Nat. Commun.* **8**, 659 (2017).
- [39] Y.-H. Song *et al.*, Observation of Coulomb gap in the quantum spin Hall candidate single-layer $1T'-\text{WTe}_2$, *Nat. Commun.* **9**, 4071 (2018).
- [40] S. Tang *et al.*, Quantum spin Hall state in monolayer $1T'-\text{WTe}_2$, *Nat. Phys.* **13**, 683 (2017).
- [41] Y. Shi *et al.*, Imaging quantum spin Hall edges in monolayer WTe_2 , *Sci. Adv.* **5**, eaat8799 (2019).
- [42] S. Wu *et al.*, Observation of the quantum spin Hall effect up to 100 Kelvin in a monolayer crystal, *Science* **359**, 76 (2018).
- [43] R. Skolasinski, D. I. Pikulin, J. Alicea, and M. Wimmer, Robust helical edge transport in quantum spin Hall quantum wells, *Phys. Rev. B* **98**, 201404(R) (2018).
- [44] J. Heising and M. G. Kanatzidis, Structure of restacked MoS_2 and WS_2 elucidated by electron crystallography, *J. Am. Chem. Soc.* **121**, 638 (1999).
- [45] G. Eda *et al.*, Coherent atomic and electronic heterostructures of single-layer MoS_2 , *ACS Nano* **6**, 7311 (2012).

- [46] K.-A. N. Duerloo, Y. Li, and E. J. Reed, Structural phase transitions in two-dimensional Mo- and W-dichalcogenide monolayers, *Nat. Commun.* **5**, 4214 (2014).
- [47] See Supplemental Material at <http://link.aps.org/supplemental/10.1103/PhysRevMaterials.3.054206> for details of the model derivation, for an analysis of the relation between edge gap and magnetic field, for details of the modeling of disordered edges, for a discussion of the limitations of the nanoribbon models, and for an analysis of the effect of bulk-parameter perturbations.
- [48] L. Muechler, A. Alexandradinata, T. Neupert, and R. Car, Topological Nonsymmorphic Metals from Band Inversion, *Phys. Rev. X* **6**, 041069 (2016).
- [49] S. Ok *et al.*, Custodial glide symmetry of quantum spin Hall edge modes in WTe_2 monolayer, *Phys. Rev. B* **99**, 121105 (2019).
- [50] I. Cucchi *et al.*, Microfocus laser-ARPES on encapsulated mono-, bi-, and few-layer $1T'$ - WTe_2 , *Nano Lett.* **19**, 554 (2019).
- [51] K. Koepnick and H. Eschrig, Full-potential nonorthogonal local-orbital minimum-basis band-structure scheme, *Phys. Rev. B* **59**, 1743 (1999).
- [52] <https://www.fplo.de>.
- [53] J. P. Perdew, K. Burke, and M. Ernzerhof, Generalized Gradient Approximation Made Simple, *Phys. Rev. Lett.* **77**, 3865 (1996).
- [54] A. Mar, S. Jobic, and J. A. Ibers, Metal-metal vs tellurium-tellurium bonding in WTe_2 and its ternary variants TaIrTe_4 and NbIrTe_4 , *J. Am. Chem. Soc.* **114**, 8963 (1992).
- [55] D. Varjas, T. O. Rosdahl, and A. R. Akhmerov, Qsymm: Algorithmic symmetry finding and symmetric Hamiltonian generation, *New J. Phys.* **20**, 093026 (2018).
- [56] L. Fu and C. L. Kane, Topological insulators with inversion symmetry, *Phys. Rev. B* **76**, 045302 (2007).
- [57] C. W. Groth, M. Wimmer, A. R. Akhmerov, and X. Waintal, KWANT: A software package for quantum transport, *New J. Phys.* **16**, 063065 (2014).
- [58] A. Lau, R. Ray, D. Varjas, and A. Akhmerov, The influence of lattice termination on the edge states of the quantum spin Hall insulator monolayer $1T'$ - WTe_2 , Zenodo (2018), doi: [10.5281/zenodo.2274694](https://doi.org/10.5281/zenodo.2274694)